Fluidization of a two-dimensional granular system: Experimental study and scaling behavior

Stephen Warr,[1] Jonathan M. Huntley,[2] and George T. H. Jacques[3]

[1]*Cavendish Laboratory, Madingley Road, Cambridge CB3 0HE, United Kingdom*

[2]*Department of Mechanical Engineering, Loughborough University of Technology, Loughborough LE11 3TU, United Kingdom*

[3]*Insignia Solutions Limited, Kingsmead Business Park, High Wycombe, Buckinghamshire, United Kingdom*

Digital high speed photography and computer image processing have been used to investigate the fluidization behavior of a two-dimensional model granular material undergoing vertical vibration. Profiles of packing fraction, speed, and velocity distribution functions are measured. The packing fraction is found to be approximately uniform in a narrow region at the base, and a Boltzmann distribution gives a good fit in the upper regions. Values for the granular temperature, as a function of height, are extracted from the distribution functions and an approximately linear decay is found. We also present results for the scaling behavior of the granular temperature and the height of the center of mass. Finally, we describe a simple theoretical analysis to investigate the origin of scaling laws.

PACS number(s): 46.10.+z, 05.60.+w, 05.40.+j

I. INTRODUCTION

In recent years a large body of literature has emerged on the physics of granular materials [1], and in particular, the vertical vibration of granular materials has been extensively studied. In the low amplitude regime, the vibrations constitute sound propagation as investigated by Liu and Nagel [2–4]. As the amplitude of vibration increases, a plethora of unusual phenomena is experimentally observed [5], including heaping and convection rolls [6,7]; and at larger vibration amplitudes, period doubling instabilities leading to both standing waves [8], and traveling waves [9], on the free surface.

A further important problem, addressed in this paper, is that of fluidization within a granular material subject to vertical vibration. Clement *et al.* [10] separated the problems of convection and fluidization by considering the vertical vibration of a one-dimensional column of N beads. A transition from a condensed phase to a fluidized phase is controlled by the relative acceleration of the driving plate. Subsequently, Luding *et al.* [11] obtained the conditions required to observe the various regimes and showed scaling relations for the height of the center of mass for the system of beads in the fluidized regime. In two dimensions, Luding, Herrmann, and Blumen [12] looked at the fluidized regime using molecular dynamics and event-driven simulation techniques. A scaling relation for the height of the center of mass was also obtained. Previous experimental studies in two-dimensional systems have only considered surface fluidization whereby a condensed phase and fluidized phase coexist [13].

Fluidization behavior can be described using the kinetic theory concept of granular temperature that is widely used in theories of rapid granular flow. The reviews by Campbell [14] and Savage [15], on computer simulation and theoretical studies, respectively, discuss the concept of granular temperature and its relevance to granular materials. To obtain granular temperatures, fluctuations in particle velocities, with respect to the center-of-mass velocity are usually measured. Techniques have been developed to measure both the translational and rotational granular temperature via noninvasive high speed photography techniques [16–18]. The term noninvasive refers to the use of photographic techniques, thus avoiding the need for probes within the granular material. Unfortunately, the glass walls will still give an additional source of energy dissipation and this is discussed in the text. When kinetic theories were applied to vibrated beds, the results suggested that fluidization is greater at the bottom than at the top [19,20]. In contrast, in an early experiment [21], where sand was vibrated in three dimensions, it was reported that fluidization was confined to the upper layers of the material. Density profiles extracted from γ-ray measurements [5] and experiments with a two-dimensional system of vertically vibrated steel spheres [13,22] also indicated that a looser packing, and hence surface fluidization, occurs near the free surface.

In this paper, rather than looking at the transitions from a condensed phase to a surface phase we consider a regime where the particles are almost entirely fluidized. In Sec. II we present the experimental method, which is a development of that in our previous work [16], which comprises a high speed photography and digital image processing technique for making noninvasive measurements of system properties such as density and granular temperature. Such experimental observations are required to test both theoretical and computer simulation studies on the physics of granular materials. The experimental results are discussed in Sec. III where we characterize the particle packing fraction and granular temperature as a function of height. We also consider the scaling behavior of the granular temperature with system size and vibration excitation peak velocity. The scaling of the height of the center of mass is also considered and comparisons are made with recent computer simulation studies. Finally, a theoretical study of the scaling law behavior is given in Sec. IV where we assume the fluidized state to be characterized by an isothermal atmosphere, i.e., a granular material with constant granular temperature.

II. EXPERIMENTAL METHODS

The experiments were performed using an electromagnetically driven shaker (Ling Dynamics Systems Model V650) driven by sine waves from a low-distortion signal generator (Farnell DSG2) and 1 kW power amplifier (LDS PA1000). The moving part of the shaker is a platform 156 mm in diameter which can attain a maximum peak to peak displacement of 25.4 mm and a maximum velocity and acceleration of 1.06 m s^{-1} and 70 g ($g = 9.81$ m s^{-2}), respectively. A cell made up of two glass plates 165 mm wide by 285 mm high was mounted on the moving platform. The width between the plates was controlled by spacers of varying thicknesses to a resolution of 0.05 mm. Chrome steel spheres, 5 mm in diameter, were used for all the experiments described here, and by adjusting the plate spacing to 5.05 mm a close approximation to an idealized two-dimensional model powder was obtained. Vertical accelerations were monitored using two Endevco Model 224 c Piezoelectric accelerometers, one attached to each side of the support; the signals were monitored by a LDS CA4 charge amplifier. Displacements of the vibrating cell were measured using a calibrated laser displacement meter (Nippon Automation LAS-5010V). This allowed the horizontal acceleration to be checked at various points (a total of eight) on the cell. The horizontal acceleration was found to be less than 2% of the vertical acceleration for the working range used in this paper, indicating an essentially one-dimensional acceleration field.

The motion of the steel spheres was filmed using a Kodak Ektapro 1000 digital high speed camera at 1000 frames s^{-1} and images were transferred to a computer, as discussed in a previous paper [16]. The system was illuminated from the rear using a stabilized halogen light source and a field lens close to the cell. Each experiment resulted in 1600 images, each 239 by 192 pixels in size, which were then downloaded to a computer (Sun IPX SPARC station). Image processing based on the Hough transform and particle tracking routines were used to give information on particle coordinates and velocities in all frames [16]. The total analysis time per set of 1600 frames (comprising downloading of frames, Hough transform analysis and tracking) was approximately 90 min. Particles with centers outside the field of view can also be detected. Particle orientations can also be detected using Hough transforms [16], but in this paper we do not consider the rotational velocities.

III. EXPERIMENTAL RESULTS AND DISCUSSION

All the experiments reported here were carried out with a sinusoidal vibration

$$y(t) = A_0 \sin(\omega t) , \tag{1}$$

where $y(t)$ is the vertical displacement of the driver base at time t, A_0 is the amplitude, and ω is the angular frequency of the vibration; here the experiments were carried out at a fixed frequency of 50 Hz. The number of spheres were varied from $N = 27$, 40, 60 up to $N = 90$, and the vibration amplitudes considered were $A_0 = 0.5$,

1.12, 1.84, and 2.12 mm. An image magnification of 13.3 pixels per ball diameter was used throughout, giving horizontal and vertical fields of view of 89.9 and 72.2 mm, respectively. The vertical range was extended by filming each combination of A_0 and N at three separate heights. The coefficient of restitution ε was measured by detecting collision events within the shaking cell [23]. The pre and postrelative velocities parallel to the line of centers was extracted and a value of $\varepsilon = 0.92$ measured. Coordinate and velocity data for each experiment was analyzed to extract data on particle packing fraction and granular temperature profiles. The results from each image were divided up into a 6×6 grid so that when data from the three different camera positions were combined, information on an 18×6 grid of cells was obtained. System properties can then be obtained within horizontal and vertical strips, grid cells, and for the entire field of view.

A. Packing fraction distributions

The particle packing fraction ϕ is defined by

$$\phi = \frac{(\text{area of particles})}{(\text{total area})} . \tag{2}$$

When particles cross grid boundaries, the number of pixels of the particle, of known radius, in each cell is counted to give the contribution of the particle area in each cell. A resolution factor, whereby each pixel is subdivided into a finer grid, is used to increase accuracy and all data is averaged over 1600 frames.

In this section we consider the regime of nearly complete fluidization rather than partial, surface fluidization, which was observed at smaller particle sizes over a similar range of frequency and amplitude of shaking. Figures 1(a)–1(d) show three-dimensional packing fraction surfaces for the case $f = 50$ Hz and $A_0 = 2.12$ mm with $N = 27$, 40, 60, and 90, respectively. The data in these figures were obtained by averaging over 1600 frames. The width profile strip axis represents variations of packing fraction between the side walls while the height profile strips show the height variation of the packing fraction. The packing fraction shows increased local fluctuations at low N which die down as N is increased. Further, no significant wall effects are evident; those in Fig. 1(a) merely reflect the large fluctuations in the packing fraction.

By averaging the plots shown in Fig. 1 along the horizontal axis, we obtain the packing fraction profiles shown in Fig. 2(a). Figure 2(b) shows similar packing fractions for $N = 90$ over the range of amplitudes from $A_0 = 0.5$ mm to $A_0 = 2.12$ mm. Error bars were found to be of the order $\phi \pm 2.5 \times 10^{-3}$ and they were therefore omitted from the figures. The data from Fig. 2(a) are replotted on log-linear axes in Fig. 2(c) and exponential decay in the tails is now clearly evident. By masking out the data points in this bottom boundary layer we can fit an exponential curve to the tail of the packing fraction profiles. Figure 2(d) shows the exponential fit to the profile for the case $N = 90$ and $A_0 = 2.12$ mm. From the decay rate in the fitted exponential we can extract a value

for the granular temperature E_0 from the experiment and use it in scaling law tests, as discussed in Sec. II B. Figure 2(a) indicates that at the base of the array the density is approximately constant with a dip at the very bottom. At constant A_0 the size of the dip and the width of the constant density region increases with larger N indicating that the system is harder to completely fluidize as N increases. For any given vibration amplitude, it is found that the height of the center of mass (obtained by integrating the packing fraction profiles) increases with decreasing N and the extent of the Boltzmann distribution fit is greater as N decreases because the system is more fully fluidized at the base. A similar increase in height dilation as N decreases, was observed in a one-dimensional column of spheres [11]. As N increases, the local packing

fraction at the base increases and hence both the collision frequency and the energy dissipation rate will increase causing less fluidization at the base.

Despite the boundary layer at the base, the exponential distribution function suggests that thermodynamic and kinetic theory concepts should be applicable, at least as a first approximation, in such granular assemblies. Energy input from the driving base and energy dissipation from inelastic collisions should balance at steady-state and quasithermodynamic concepts like granular temperature and packing fraction, and kinetic pressure may enable such systems to be characterized. Bernu, Delyon, and Mazighi [24] solved the dissipative Boltzmann equation, in the limit of low dissipation, for a one-dimensional array of spheres and found a density profile which was
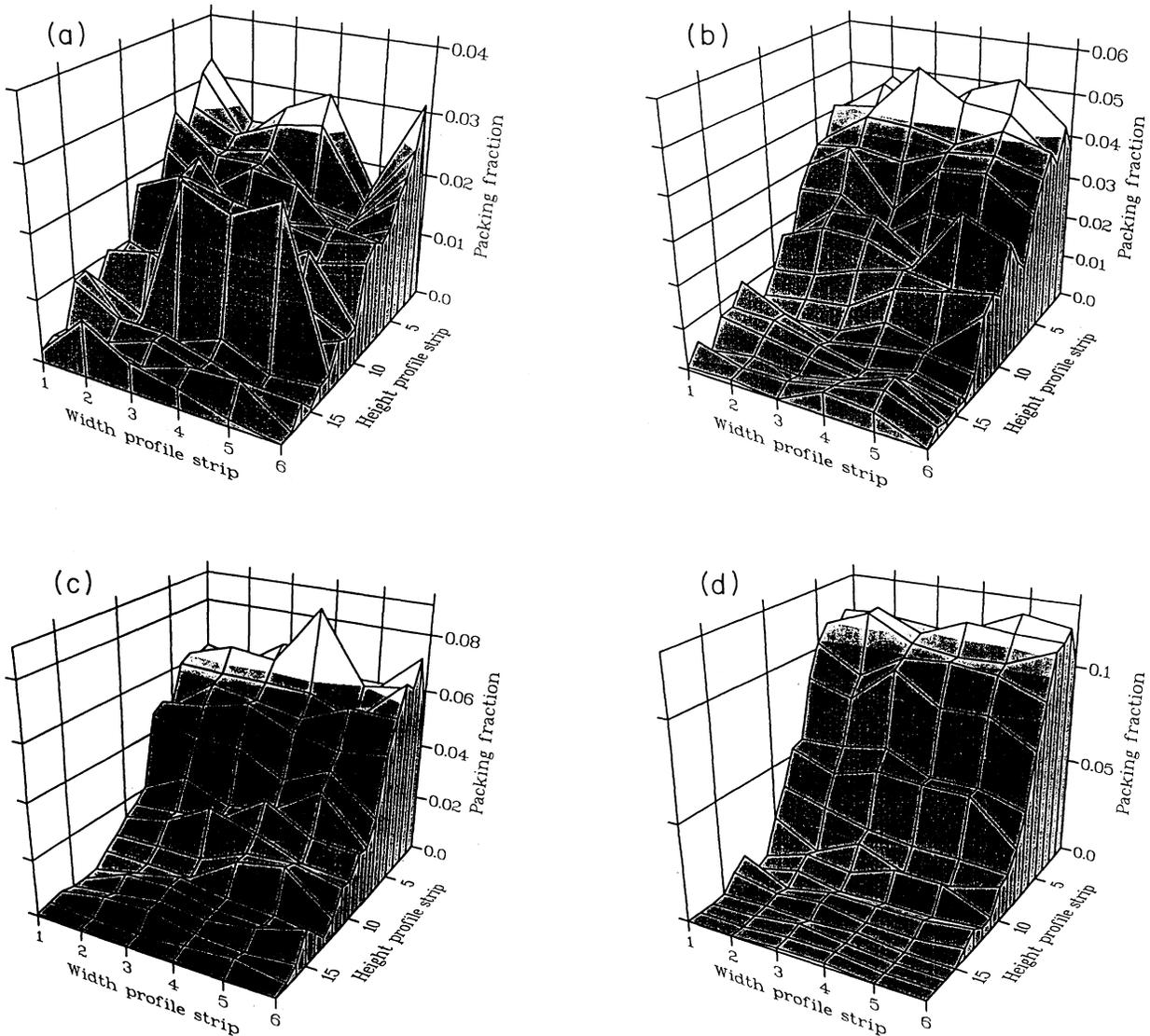

FIG. 1. Three-dimensional packing fraction surfaces based on an 18×6 grid for the case $f=50$ Hz and $A_0=2.12$ mm with (a) $N=27$, (b) $N=40$, (c) $N=60$, and (d) $N=90$.

nearly exponential. Such a calculation for a two-dimensional system would be difficult and it has not been attempted as far as we are aware. Experimental and simulation data in one dimension [11] shows evidence for exponential distributions and simulations in two dimensions [12] found deviations from the exponential attributed to inelastic collisions. Further work is required to see over what range of the parameter space in one and two dimensions such distributions are exhibited.

B. Velocity distributions

Granular temperatures are measured by constructing velocity and speed distribution functions and fitting Maxwell and Rayleigh distribution functions to the data [16]. To measure granular temperature profiles, distribution functions are generated using velocity data from particles whose centers lie within a strip or cell. The granular temperature of a strip or cell is then obtained from the best fit from that strip or cell.

We next consider the distribution functions for particle x and y velocities from which we can extract a value for

the x and y components of the granular temperature tensor, in order to probe further the thermodynamic nature of these systems. Here, the x and y degrees of freedom are tangential and normal, respectively, to the direction of shaking, which is vertical. In Sec. II C, we explore the scaling law behavior of the system bulk granular temperature which is obtained by measuring the distribution functions for the entire field of view. Here, we make a preliminary exploration of the height dependence of the granular temperature to see whether the isothermal atmosphere provides a useful model for describing the systems. In Figs. 3 and 4 we show examples of the velocity distribution functions at various heights in the cell for the case of $N=90$ and $A_0=2.12$ mm. Figures 3(a)–3(c) shows the x-velocity distributions for strips 1, 6, and 11, with strip 1 at the bottom of the cell and Figs. 4(a)–4(c) show the corresponding y-velocity distributions in the same strips. In all cases the width of the profile strips is 32 pixels. The combination of the small number of particles N the exponential decay of packing density with height, and the fact that the images were subdivided into strips to improve spatial resolution meant that it was
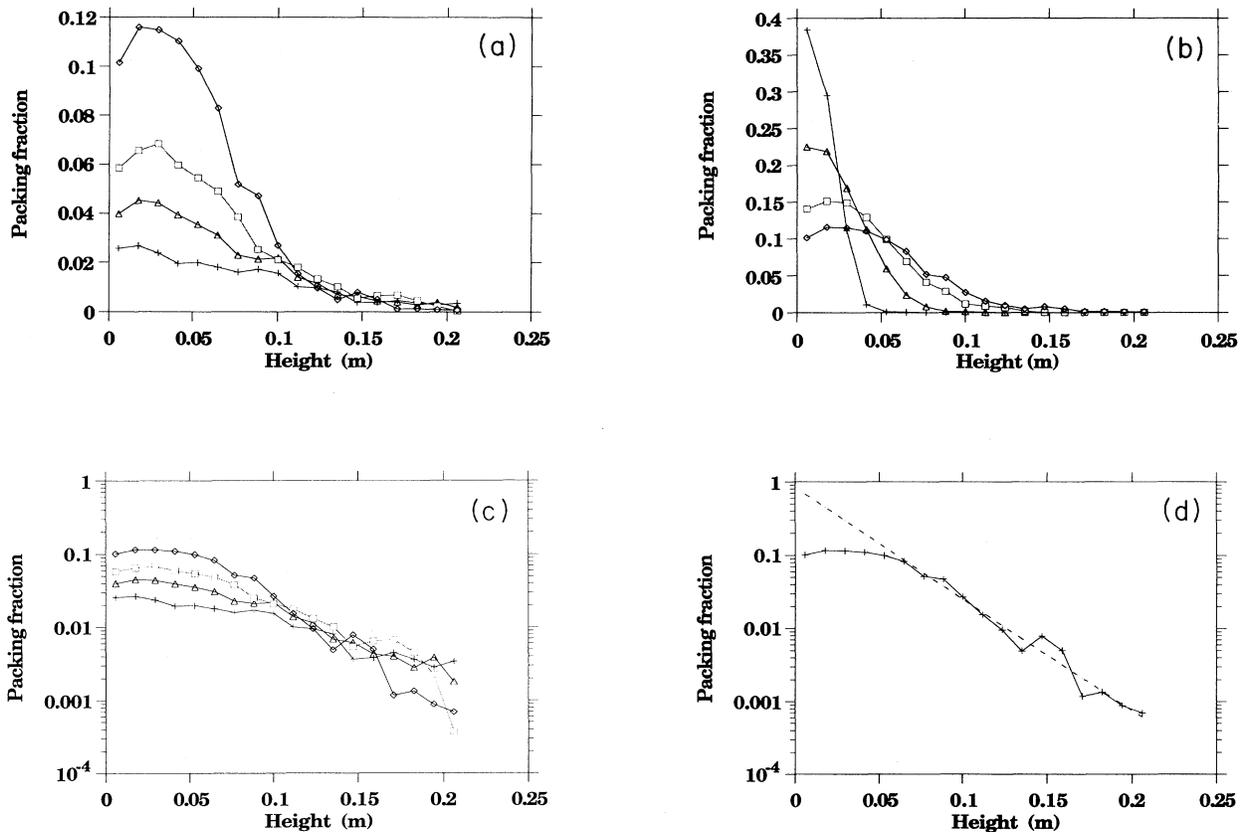

FIG. 2. (a) Effect of system size on the average packing fraction profiles. Crosses, triangles, squares, and diamonds correspond to $N=27$, 40, 60, and 90, respectively, all with $A_0=2.12$ mm. (b) Effect of vibration amplitude on the average packing fraction profiles for $N=90$. Crosses, triangles, squares, and diamonds correspond to $A_0=0.5$, 1.123, 1.84, and 2.12 mm, respectively. (c) Profiles in (a) plotted on a log-linear scale. (d) Boltzmann distributions, Eq. (5), fitted to the exponential tails of (c).

necessary to use a small number of bins and a large bin-ning interval. For all distribution function profiles we used 20 bins and an x and y velocity interval of 0.297 m s^{-1}. These values contrast with the typical 1000 bins with intervals of the order 10^{-3} m s^{-1} used with denser systems [16]. The general trend from these figures is that the distributions become narrower as one moves up to higher strips. This indicates a decrease in the granular temperature with height, as will be seen shortly.

A number of issues relating to these distribution func-tions need to be raised at this point. The concept of granular temperature is normally associated with veloci-ties which are measured with respect to the center-of-mass velocity v_{cm}. This velocity is, however, difficult to
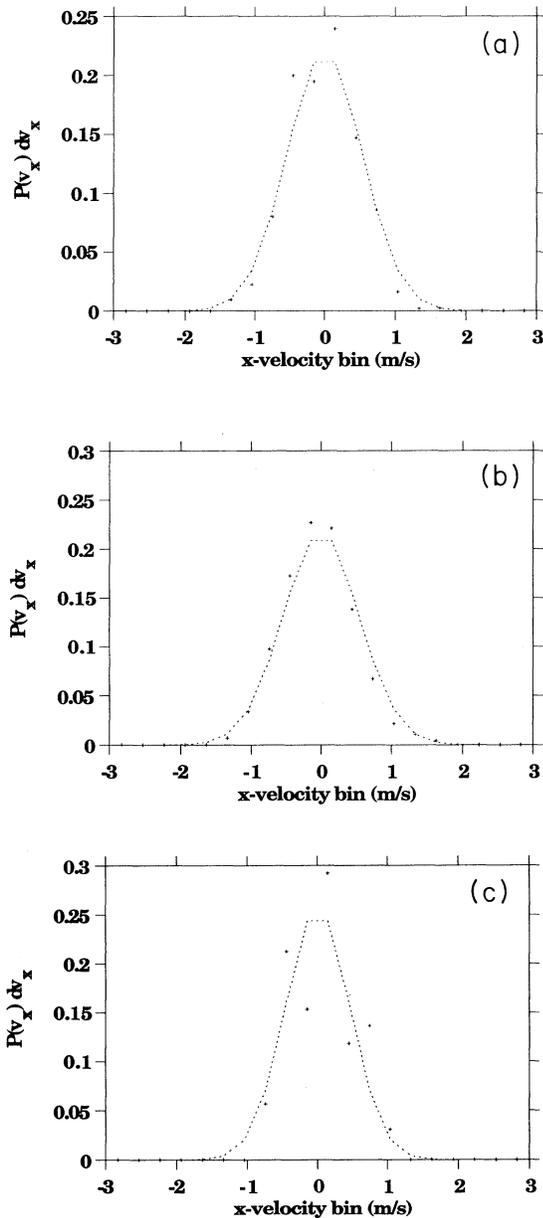

FIG. 3. Horizontal strip profiles of the v_x distribution func-tions for $N=90$ and $A_0=2.12$ mm. 20 v_x bins, each of width 0.297 m s^{-1}, were used in the distributions and the height of the profile strips is 32 pixels. Distributions are plotted for (a) strip 1 with a midpoint height of 5.89 mm; (b) strip 6 at 64.77 mm; (c) strip 11 at 123.65 mm. Crosses correspond to data points and the dashed line is the best fit Gaussian curve.
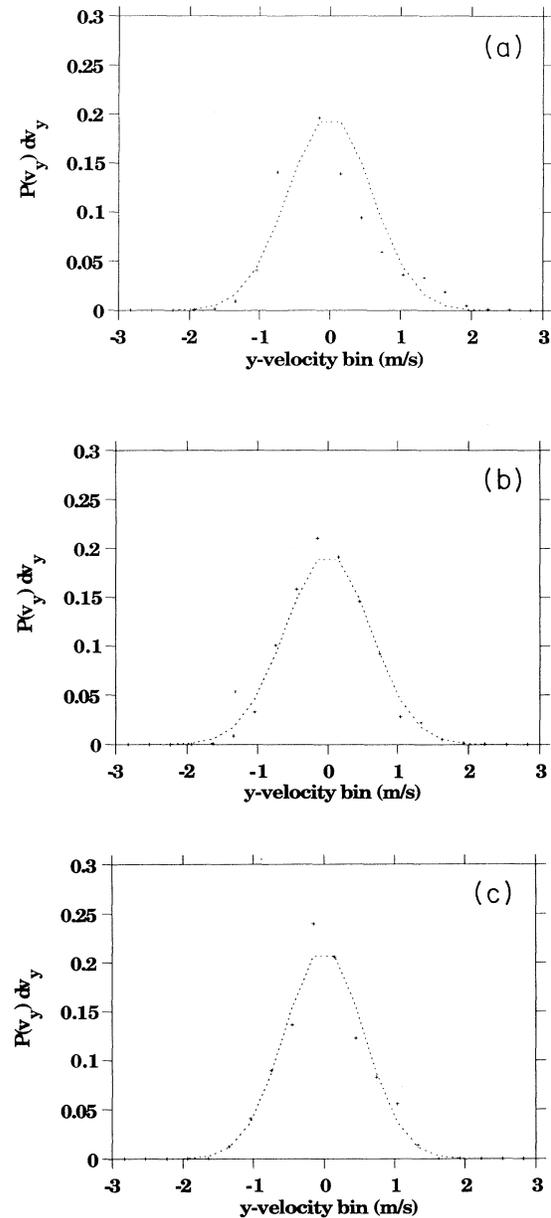
FIG. 4. Horizontal strip profiles of the v_y velocity distribu-tion functions for $N=90$ and $A_0=2.12$ mm. 20 v_y bins, each of width 0.297 m s^{-1}, were used in the distributions and the width of the profile strips is 32 pixels. Distributions are plotted for (a) strip 1 with a midpoint height of 5.89 mm; (b) strip 6 at 64.77 mm; (c) strip 11 at 123.65 mm. Crosses correspond to data points and the dashed line is the best fit Gaussian curve.
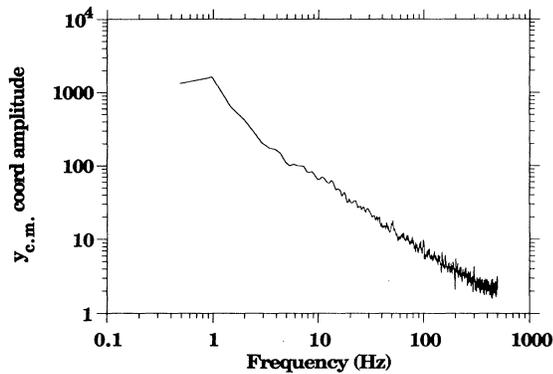
FIG. 5. Amplitude spectrum obtained from FFT analysis of the y-center-of-mass coordinate data over 1600 frames for the case $N=90$ and $A_0=2.12$ mm.

ity of that particle and the fluctuation velocity would then be calculated to be zero. Even with averaging over several frames and cycles, significant distortions to the distributions are produced by this effect. To make any progress, all distribution functions use velocities measured in the absolute reference frame and choosing a higher vibration frequency of 50 Hz ensures the system of spheres behaves like a fluidized gas with limited fluctuation in the center-of-mass velocity. We have checked to see if the center-of-mass (c.m.) coordinate exhibits any harmonics or subharmonics of the driving frequency by computing the amplitude spectrum of the center-of-mass data. We computed the fast Fourier transform (FFT) of the data using each of the 1600 frames. An amplitude spectra for the y center-of-mass (c.m.) coordinate is shown in Fig. 5 for $N=90$ with $A_0=2.12$ mm. The spectra shows no evidence of excess energy in any harmonics related to the driving frequency or any other frequency. There is a small peak close to 50 Hz which increases in height as N decreases; for example, the energy in the harmonics around 50 Hz for the x-c.m. coordinate is 0.02 and 0.05 % of the total energy (over 0 to 500 Hz frequency range), respectively, for $N=90$ and $N=27$. For the y-c.m. coordinates the corresponding percentages are, respectively, 0.01% and 0.1%. The approximation

measure in the case of low N and large number of strips since only a small number of particles (sometimes less than one) will be in each strip on any one frame. Estimation of $v_{c.m.}$ by averaging the velocities within a strip therefore results in a significant bias. In the limiting case of a single particle, $v_{c.m.}$ would be calculated as the veloc-
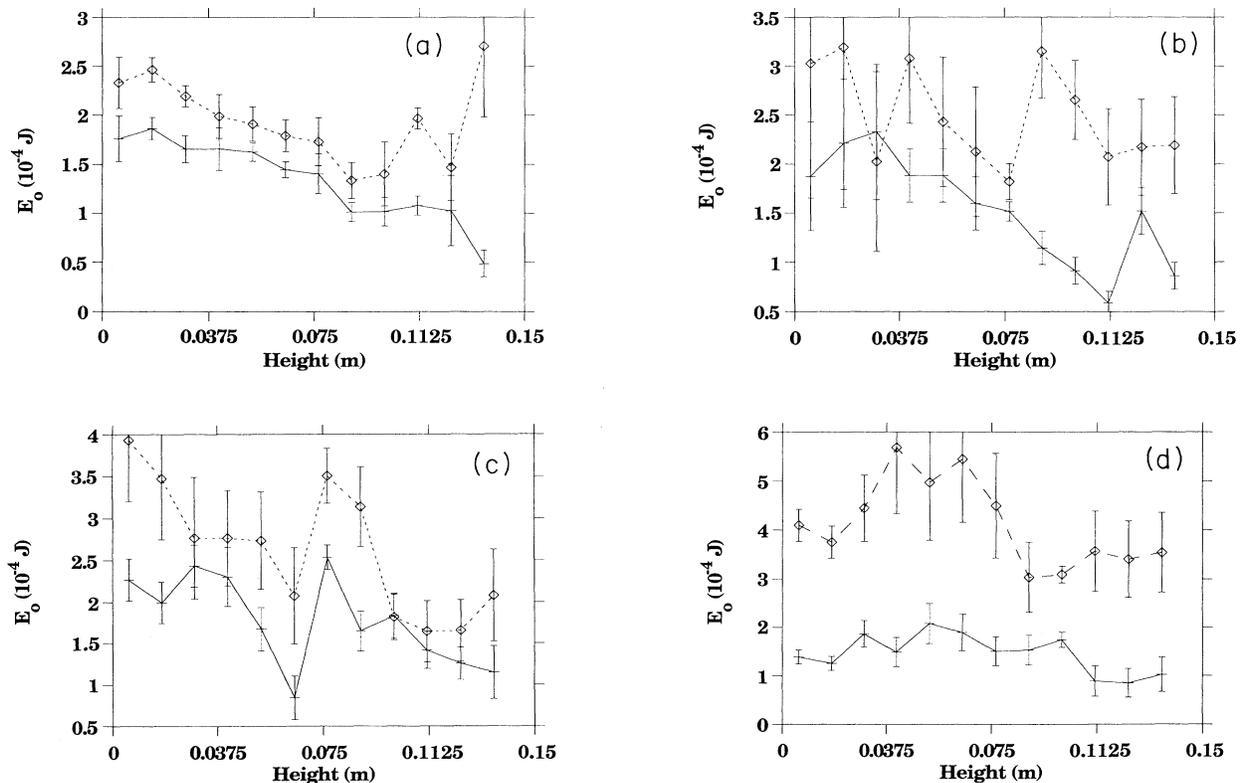

FIG. 6. Horizontal profiles of granular temperature where E_0 has been extracted from the best fit Gaussians to the velocity distributions. $A_0=2.12$ mm and $N=$ (a) 90; (b) 60; (c) 40; (d) 27. Crosses and diamonds correspond to the x and y components of the granular temperature, respectively.

of using absolute velocities rather than velocities in the center-of-mass frame is therefore a reasonable one.

One consequence of the absolute reference frame is the distortion of the y-velocity distribution in the bottom few strips due to the effect of the driving base as can be seen in Fig. 4(a). By strips 5 and 6 this distortion in the y-velocity distribution has nearly gone, as Fig. 4(b) shows. From strips 1 to 10 the x velocities are well approximated by a Gaussian but with slight distortion in the bottom strips. In some cases slight departures from a Gaussian can be seen in one or both tails. The nature and reasons for non-Gaussian velocities has become a subject of some debate [25–27]; at present we do not consider the fine detail of the velocity distributions but consider the Gaussian to be a good approximation to the data from which granular temperatures can be extracted. As one moves towards the upper strips the ability to measure velocity distributions from 1.6 s worth of data starts to break down; strip 11, for example, contains 880 particles over 1600 frames. In Fig. 3(c) an insufficient number of independent velocities means we have too many bins for the number of velocities and the scatter becomes much larger. In Fig. 4(c) the y-velocity distribution is fit well by a Gaussian so N is still large enough to obtain good statistics. Above strips 11 and 12 however, the distributions break down and no fitting was attempted in any strips beyond number 12 even though particles were found in a further six strips. At these low N values the changes in the distribution functions are only slight; at larger N and higher densities more pronounced changes are clearly visible.

Using the velocity distribution function profile data we extracted the granular temperature as a function of height (see Ref. [16] for details where we take the particle mass to be 4.79×10^{-4} kg). Figures 6(a)–6(d) show both the x and y components of the granular temperature as a function of height for $N = 90$, 60, 40, and 27, all at a vibration amplitude of $A_0 = 2.12$ mm. Fluctuations occur due to the small numbers of particles within each analysis area; the error bars were therefore estimated by calculating the root mean square granular temperature fluctuation as a function of sample size at higher density regions of the cell. All the profiles show that the granular temperatures are anisotropic over the entire height. The reason for this may be that the driving base generates an initially anisotropic collective motion within the cell and the collisions are unable to completely randomize the motion. It is possible to observe almost completely isotropic velocities in the center-of-mass frame [13,28] but here the degree of anisotropy is sufficiently small that we can characterize the systems by a granular temperature given by the trace of the tensor components. In such cases the speed distribution functions are closely approximated by the Maxwell-Boltzmann distribution function, as shown in Fig. 7 which shows the speed distribution in strip one for $N = 90$ and $A_0 = 2.12$ mm. When the degree of anisotropy becomes large a characteristic deviation from the Maxwell-Boltzmann distribution is observed [28]. Qualitative observation of the profiles in Fig. 6 suggests that the granular temperature decays approximately linearly with height. At present the statistics are uncer-
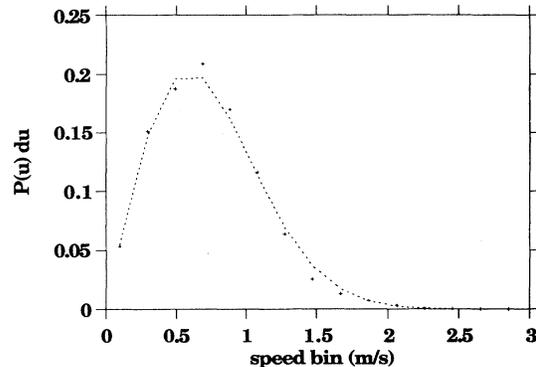

FIG. 7. Speeds fitted by the Maxwell-Boltzmann distribution function for strip one with $N = 90$ and $A_0 = 2.12$ mm. The degree of anisotropy present in these systems is not sufficient to cause a noticeable deviation from the theoretical form. The small deviations are caused by the slight distortions from the Gaussian in the velocity fits.

tain and we have not been able to extract any meaningful correlation of the decay rate of granular temperature with amplitude and system size. Detailed theoretical work is needed to determine the height dependence of the granular temperature for a system with dissipative collisions.

C. Experimental tests of scaling laws

Following the recent publication of a scaling analysis and experimental study on a one-dimensional column of spheres [11] and computer simulation studies of similar scaling behavior in a two-dimensional array of spheres [12], we next present experimental results which test these scaling predictions. In Sec. IV we consider a simple theoretical analysis in an attempt to derive the form of the scaling law from first principles. The scaling law proposed for a two-dimensional system by Luding, Herrmann, and Blumen [12] takes the form

$$h_{c.m.} - h_{c.m.,0} \approx (A_0 \omega)^{1.5} X^{-1} , \qquad (3)$$

where $h_{c.m.}$ is the height of the center of mass, $h_{c.m.,0}$ is the height of the assembly of beads at rest, and $X = (N/n_b)(1 - \varepsilon)$ is an effective dissipation parameter. An expression for $h_{c.m.,0}$ is given as

$$h_{c.m.,0} = \frac{n_b d}{2N}[(1 - \sqrt{3}/2)n_h + (\sqrt{3}/2)n_h^2]$$

$$+ \frac{n_0 d}{2N}[1 + \sqrt{3}n_h] , \qquad (4)$$

where $n_b = L/d - 0.5$ is the average number of beads per layer in a cell of width L, and d is the bead diameter. The other terms are $n_h = n$ int(N/n_b) which is the number of full layers and $n_0 = N - n_h n_b$ which is the number of beads in the final layer.

We investigate the scaling behavior in three ways: first, by using the value of the granular temperature (denoted

here by E_0) extracted from the bulk speed distribution functions from the bottom camera position (i.e., strips one–six inclusive); second, by using the value of E_0 extracted from the exponential fit to the tails of the packing fraction profiles; and third, by extracting the height of the center of mass from the packing fraction profiles in order to make a direct comparison with the results of Luding, Herrmann, and Blumen [12].

In the first case the bulk distribution functions were based on 50 bins with binning intervals for speeds and velocities of 0.131 m s^{-1} and 0.198 m s^{-1}, respectively. As stated earlier, velocities are measured in the absolute reference frame without subtracting the center-of-mass velocity. A small degree of skew exists in some v_y distributions and the v_x distributions are well approximated by Gaussians. The scaling analysis is based on E_0 values from the speed fits (rather than v_x and v_y fits) because these average out the small degree of anisotropy present and are less affected by small distortions from the Gaussians. The distribution functions are evaluated for each of the four system sizes and four vibration amplitudes, all at a frequency of 50 Hz. For increasing amplitudes, the nondimensional accelerations $\Gamma = A_0\omega^2/g$ are, respectively, 5.03, 11.23, 18.37, and 21.33. Figures 8 and 9 show the scaling of E_0 with the characteristic velocity $A_0\omega$ and system size n_b/N, respectively. Power law curves have been fitted to these data sets and the exponents are given in the captions. From the figures the average exponent for the $A_0\omega$ scaling is 1.41 ± 0.03 and that for the n_b/N scaling is 0.6 ± 0.03. In Figs. 10 and 11 we scale out the effects of system size and characteristic velocity, respectively, using the average exponents. The scaling with $A_0\omega$ is quite good although the exponent of 1.41 ± 0.03 is slightly below the value of 1.5 found by Luding, Hermann, and Blumen [12], for the scaling of the center of mass. The scaling with n_b/N is poorer with the data at the largest amplitude showing the greatest devia-
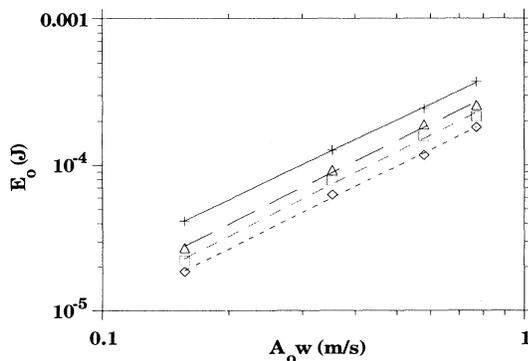

FIG. 9. Granular temperature E_0 as a function of n_b/N with E_0 measured from bulk speed distribution functions. Crosses, triangles, squares, and diamonds correspond to $A_0=0.5$, 1.12, 1.84, and 2.12 mm, respectively. Power law fits shown in the figures $(n_b/N)^\beta$ give exponents of $\beta=0.65$, 0.57, 0.59, and 0.58, respectively, for each of the above cases.

tions. Again the exponent of 0.6 ± 0.03 is somewhat less than the value of one in [12].

The second scaling analysis used E_0 values extracted from exponential fits to the tails of the packing fraction profiles (as outlined in Sec. III B). Figures 12 and 13 show the scaling plots in this case. Results for the $A_0\omega$ scaling are very poor here and no fitting was attempted; for the n_b/N scaling the results approximately scale except for the smallest amplitude, and the exponents are given in the figure caption and are closer to 1.0 than the previous values.

We finally try and make a direct comparison with the results of Luding, Herrmann, and Blumen [12] by looking at the scaling of the height of the center-of-mass velocity. In Ref. [12], $h_{c.m.} - h_{c.m.,0}$ is considered where $h_{c.m.}$ is the height of the center of mass of the array of spheres during vibration and $h_{c.m.,0}$ is the corresponding height

FIG. 8. Granular temperature E_0 as a function of $A_0\omega$ with E_0 measured from bulk speed distribution functions. Crosses, triangles, squares, and diamonds correspond to $N=27$, 40, 60, and 90, respectively. Power law fits shown in the figures $(A_0\omega)^\alpha$ give exponents of $\alpha=1.36$, 1.43, 1.45, and 1.41, respectively, for each of the above cases.
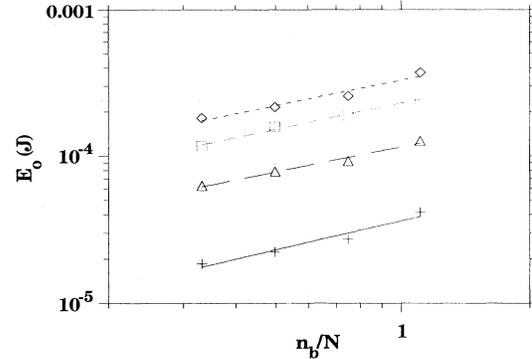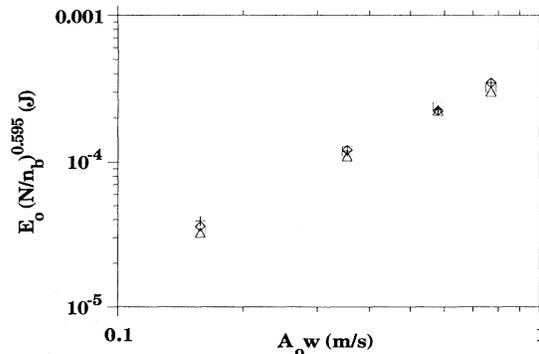

FIG. 10. Granular temperature E_0 as a function of $A_0\omega$ with the effects of system size scaled out using the average exponent $\beta=0.60$ from Fig. 9. Crosses, triangles, squares, and diamonds correspond to $N=27$, 40, 60, and 90, respectively.
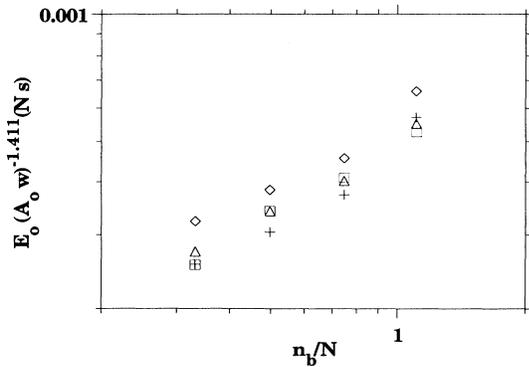
FIG. 11. Granular temperature E_0 as a function of n_b/N with the effects of the characteristic velocity $A_0\omega$ scaled out using the average exponent $\alpha = 1.41$ from Fig. 8. Crosses, triangles, squares, and diamonds correspond to $A_0 = 0.5$, 1.12, 1.84, and 2.12 mm, respectively.

FIG. 13. Granular temperature E_0 as a function of n_b/N with E_0 measured from exponential Boltzmann distributions fitted to the tails of the packing fraction profiles. Crosses, triangles, squares, and diamonds correspond to $A_0 = 0.5$, 1.12, 1.84 and 2.12 mm, respectively. Power law fits to the diamond and triangle data give exponents of $\beta = 0.75$ and 0.85, respectively.

of the array at rest calculated using Eq. (4). The initial configuration of spheres is only partially visible within the camera's field of view. Excluding a boundary next to the walls and driving base from the field of view prevents problems with the particle tracking. The datum level of the camera base was set to be 5 mm from the base of the cell at rest; this means that $h_{c.m.,0}$ can be negative with respect to this datum in some cases. $h_{c.m.}$ is found by integrating the packing fraction profile data according to Eq. (25) of this paper. The packing fraction data were extrapolated to account for the fact that strip 1 excludes the base of the cell. Figures 14 and 15 show the $A_0\omega$ and n_b/N scaling, respectively, for $h_{c.m.} - h_{c.m.,0}$. From Fig. 14 the data scales consistently apart from the case with $N = 90$ and the average exponent for the lower three cases is 1.3 ± 0.04, which is lower than the expected value of
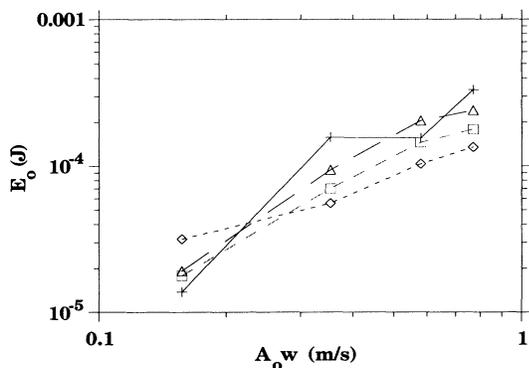
1.5 in [12]. In Fig. 15 the scaling is crude and gives an average exponent of 0.27 ± 0.11.

There are a number of reasons why the above three methods give different values for the scaling exponents. The main reason is that they would be expected to give the same answer for a nondissipative isothermal atmosphere, but since this situation does not prevail differences are not surprising. There are, however, perturbations on the system due to the mechanics of the experiment. The two-dimensional nature of the experimental setup results in additional forces above those encountered in particle-particle collisions. The main concern is particle-wall friction at the glass walls generated through particle-wall collisions. Electrostatic forces are negligible (the particle material and size ensure this) and we have not considered the effect of air drag which is not expected

FIG. 12. Granular temperature E_0 as a function of $A_0\omega$ with E_0 measured from exponential Boltzmann distributions fitted to the tails of the packing fraction profiles. Crosses, triangles, squares, and diamonds correspond to $N = 27$, 40, 60, and 90, respectively. No power law fitting was attempted for these data.
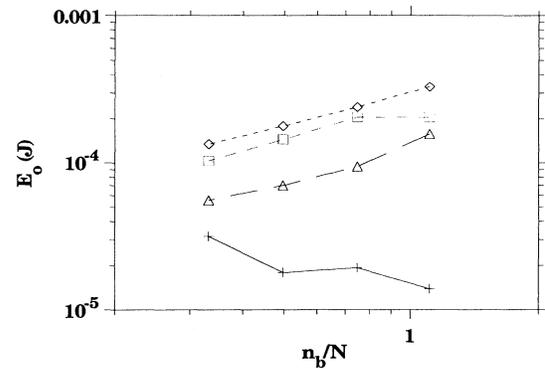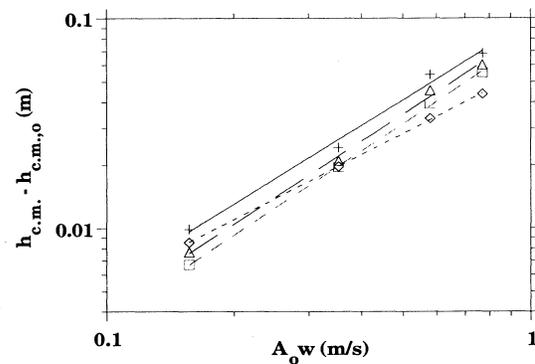

FIG. 14. $h_{c.m.} - h_{c.m.,0}$ as a function of $A_0\omega$. Crosses, triangles, squares, and diamonds correspond to $N = 27$, 40, 60, and 90, respectively. Power law fits of the form $(A_0\omega)^\alpha$ are shown in the figure and the exponents were $\alpha = 1.24$, 1.31, 1.33 and 1.02, respectively.
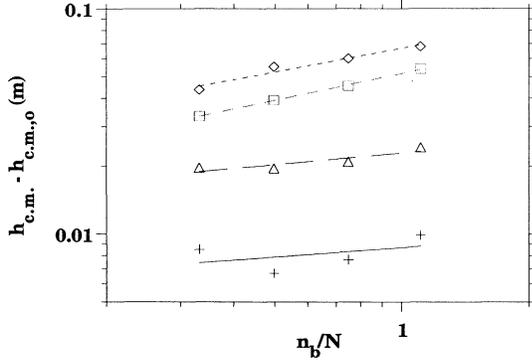
FIG. 15. $h_{c.m.} - h_{c.m.,0}$ as a function of n_b/N. Crosses, triangles, squares, and diamonds correspond to $A_0 = 0.5$, 1.12, 1.84, and 2.12 mm, respectively. Power law fits of the form $(n_b/N)^\beta$ are shown in the figure and the exponents were $\beta = 0.14$, 0.17, 0.40 and 0.35, respectively.

to significantly affect the results. In order to estimate the energy loss through particle-wall collisions we apply the analysis of Drake [18]. The energy dissipated per particle per unit time by particle-wall collisions is given by

$$\Delta E_w = \frac{1}{3}\left[\frac{1+\varepsilon}{\sigma\gamma}\right]^2\left\{\frac{\ln(\gamma(1-\varepsilon)+1)}{\ln(1/\varepsilon)}\right\}^2 \mu m s U T , \qquad (5)$$

where ε is the restitution coefficient, σ is the particle diameter, μ is the coefficient of friction between the particles and glass, m is the particle mass, $s = t - \sigma$ is the difference between the glass spacing and the particle size, $2T$ is the mean of the squared particle speed, and U is a mean speed if bulk flow occurs. The dimensionless parameter γ is given by

$$\gamma = \frac{w_0\xi}{s(2T)^{0.5}} , \qquad (6)$$

where w_0 is a typical average speed of a particle normal to the sidewalls, immediately following a particle-particle collision, and ξ is the mean free path between particle-particle collisions. Equation (6) can be interpreted as a ratio of particle-wall collision rate to particle-particle collision rate. Equation (5) assumes that over a mean free path the particle collides between the two glass walls at a certain rate. The maximum magnitude of the frictional forces arising from particle-wall collisions and the energy expended working against them can be estimated if one assumes that the particles slide against the walls during the collision. The energy dissipated per particle per unit time can then be used to calculate the average energy dissipated over a typical particle trajectory.

Two examples are considered: first, $N = 27$, $A_0 = 2.12$ mm at the middle camera position, and second, $N = 90$, $A_0 = 2.12$ mm at the bottom camera position. In case I, we find five particles per frame on average and measure a mean trajectory length of 0.016 m, a mean of the squared speed of 0.941 m^2 s^{-2}, and a mean time for a trajectory of 0.017 s. Taking $m = 5.04\times10^{-4}$ kg, $\varepsilon = 0.92$,

$\mu = 0.22\pm0.03$, $s = 5.0\times10^{-5}$ m, $\sigma = 5.0\times10^{-3}$ m, and $U = T^{0.5}$, Eq. (5) gives $\Delta E_w = 4.3\times10^{-5}$ J s^{-1}. With an average trajectory lasting 0.017 s, this gives the average energy dissipated at the walls over a typical trace of 7.3×10^{-7} J. To estimate the energy loss in a particle-particle collision, we approximate the relative velocity of the particles by $\sqrt{2}\bar{u}$ where $\bar{u}$ is the mean speed and the average energy lost in a single collision is then [18]

$$\Delta E_c \approx \frac{1}{4}mv^2(1-\varepsilon^2) = \frac{1}{2}m\bar{u}^2(1-\varepsilon^2) = \alpha m\bar{u}^2 , \qquad (7)$$

where the mean of the square relative velocity of colliding particles v^2 is approximated as above. In case I, Eq. (7) gives $\Delta E_c = 3.6\times10^{-5}$ J which is approximately 10% of the granular temperature. The energy loss at the walls for a typical trajectory is therefore estimated to be 2% of the energy lost in an average collision.

Case II is a denser system with an average of 42 particles per frame and mean trajectory length of 0.0054 m, a mean squared speed of 0.73 m^2 s^{-2}, and mean time for a trajectory of 0.0063 s. Using the above parameters in Eq. (5) gives $\Delta E_w = 5.3\times10^{-5}$ J s^{-1} and an average energy dissipated at the walls over a typical trace of 3.3×10^{-7} J. The energy lost in an average collision is $\Delta E_c = 2.8\times10^{-5}$ J which then gives an estimate of the energy lost at the walls as 1.2% of the energy lost in a collision.

The energy losses calculated above are only approximate, but are nevertheless sufficiently low to indicate that wall friction will only be a minor perturbation for the experiments described here. The calculations show that greater particle-wall frictional damping occurs as $A_0\omega$ increases and this would be expected to reduce the granular temperature over the expected value. Particle-wall friction may therefore be responsible for the scaling exponent of $A_0\omega$ being less than the value of 1.5 found in computer simulation studies.

IV. THEORETICAL DERIVATION OF SCALING LAWS

We next consider a simple kinetic theory treatment of the fluidized regime which attempts to derive the scaling relationships demonstrated in the previous sections. We consider a two-dimensional cell of unit width, $W = 1$, with the vertical axis denoted by y. The cell contains N spheres which are vertically vibrated by a driving base at angular velocity ω and amplitude A_0. We assume that the N spheres are in a fluidized state which, to an initial approximation, can be characterized as an isothermal atmosphere. If $n(y)$ is the number of spheres per unit area at height y then the total number of particles between y and $y + dy$ is given by $Wn(y)dy$. In an isothermal atmosphere, the number density is given by the Boltzmann distribution

$$n(y) = n(0)e^{-mgy/kT} . \qquad (8)$$

By equating the integral of $Wn(y)dy$ over the range

$[0, \infty)$ to the number of spheres N we obtain

$$n(y) = \frac{mgN}{kTW} e^{-mgy/kT} . \tag{9}$$

Here, because we assume an isothermal atmosphere, we denote the granular temperature by kT rather than E_0. In two dimensions, the granular temperature, here referred to by kT rather than E_0, is related to the mean of the square of the speed through the equipartition theorem giving

$$\frac{m\overline{c^2}}{2} = kT . \tag{10}$$

From simple kinetic theory, the mean free path λ and collision frequency Z for a single sphere, in two dimensions, are given, respectively, by

$$\lambda = \frac{1}{2nd} \tag{11}$$

and

$$Z = \frac{\overline{c}}{\lambda} = 2\overline{c}nd , \tag{12}$$

where d is the sphere diameter.

We assume that the average energy lost per collision is given by $\alpha m\overline{c^2}$ where α is a dissipation coefficient given in Eq. (7). The average energy dissipated per unit time $\dot{E}$ for a single particle at height y is given by the average energy lost per collision multiplied by the collision frequency. This gives

$$\dot{E} = 2\alpha m\overline{c^2}cnd \tag{13}$$

and substituting Eqs. (9) and (10) into Eq. (13) gives

$$\dot{E} = \frac{4\alpha \overline{c}dmgN}{W} e^{-mgy/kT} . \tag{14}$$

The rate of energy dissipation $\dot{E}^D$ between heights y and $y + dy$ is then the total energy dissipated per unit time for a single particle multiplied by the number of particles between y and $y + dy$; therefore using Eqs. (14) and (9) gives

$$\dot{E}^D = \frac{4\alpha \overline{c}dmgN}{W} e^{-mgy/kT} \frac{mgN}{kTW} e^{-mgy/kT} dzW . \tag{15}$$

Integrating Eq. (15) over the interval $[0, \infty)$ leads to the total rate of energy dissipation $\dot{E}^T$ given by

$$\dot{E}^T = \frac{2\alpha \overline{c}dmgN^2}{W} . \tag{16}$$

We now consider the rate at which energy is put into the system. To simplify the analysis, we make a number of assumptions. First, we assume that energy dissipation through particle-particle collisions is more important than that through particle-base collisions and therefore we consider the case that the restitution coefficient for particle-base collisions is $\varepsilon = 1$. We also approximate the sinusoidal oscillating base by a sawtooth with amplitude sufficiently small that the velocity of a particle coming down will not change appreciably due to the effect of gravity over a distance equal to the amplitude. Further,

the frequency of the base is so high that the particle coming down sees the base moving at a velocity which is uncorrelated with the value on previous collisions.

In the laboratory reference frame, we denote the precollisional velocity of a particle by v and the base velocity by V. The definition of the restitution coefficient then leads to the postcollisional velocity for the particle, in the y direction, as being $(1+\varepsilon)V - \varepsilon v$ with the x velocity unchanged. There are two cases to consider. First, when the base moves upwards with a velocity V we have, for the particle velocity, taking $\varepsilon = 1$ and upwards as positive

$$v_{\text{before}} = \begin{bmatrix} v_x \\ -v_y \end{bmatrix} \quad v_y \geq 0 ,$$

$$v_{\text{after}} = \begin{bmatrix} v_x \\ v_y + 2V \end{bmatrix} .$$

The change in kinetic energy of the particle is then

$$\Delta(\text{KE}) = \frac{m}{2}(4V^2 + 4v_y V) \geq 0 . \tag{17}$$

The second case to consider is the base moving downwards with velocity V where the particle velocity now becomes

$$v_{\text{after}} = \begin{bmatrix} v_x \\ v_y - 2V \end{bmatrix} ,$$

and the change in kinetic energy is then

$$\Delta(\text{KE}) = \frac{m}{2}(4V^2 - 4v_y V) \leq 0 . \tag{18}$$

The change in kinetic energy has to be less than zero in this case because we must have $v_y \geq V$ for the particle to catch the base. A net gain of energy therefore results on average from these equations. If $v_y \leq V$ then case one always occurs resulting in an increase in kinetic energy. We further argue that case one is more likely than case two, which requires $v_y \geq V$ for any energy change. This can be seen by considering the probabilities of cases I and II, denoted by P_1 and P_2, respectively, which are given by

$$P_1 = \begin{cases} 1 & (v_y \leq V) \\ \dfrac{1}{2}\left[1 + \dfrac{V}{v_y}\right] & (v_y \geq V) \end{cases} \tag{19}$$

$$P_2 = \begin{cases} 0 & (v_y \leq V) \\ \dfrac{1}{2}\left[1 - \dfrac{V}{v_y}\right] & (v_y \geq V) . \end{cases} \tag{20}$$

In practice, $\omega = 50 \times 2\pi$ rad s^{-1} and the maximum value of A_0 is 2.12 mm so that $V_{\text{max}} = 0.67$ m s^{-1}. A comparison with the Gaussian distributions in Fig. 4 suggests that about half the particles have $|v_y| \leq 0.67$ m s^{-1}, and Eq. (19) shows that, of the remainder, the majority will also be governed by case I. With the aim of achieving a simple solution, we make the approximation of treating

all the collisions as case I and also neglect the term $4v_y V$. We therefore approximate the increase in kinetic energy to be a constant, given by

$$[\Delta(\text{KE})]^{\text{net}} = 2mV^2 . \qquad (21)$$

The rate of energy input into the system $\dot{E}^I$ is then given by the number of collisions with the base per unit time $(1/4)n_0\bar{c}W$ multiplied by the net increase in energy per collision, on average. We thus have

$$\dot{E}^I = \frac{n_0\bar{c}}{2} WV^2 m . \qquad (22)$$

Balancing the energy input and the energy dissipated, through equating Eqs. (22) and (16), then leads to the relation

$$kT = \frac{mV^2 W}{2\alpha d N} . \qquad (23)$$

Approximating the dissipation coefficient α by $\alpha \approx (1-\varepsilon^2)$ which is approximately $2(1-\varepsilon)$ for $\varepsilon \approx 1$ then gives

$$kT \approx \frac{mV^2 W}{4N(1-\varepsilon)d} . \qquad (24)$$

This gives a relationship for how kT scales with N, the characteristic base velocity V, the particle diameter d, and the restitution coefficient ε. These scaling predictions also apply to the center of mass of the N particles; using Eq. (8) for $n(y)$, the center-of-mass height $h_{\text{c.m.}}$ given by

$$h_{\text{c.m.}} = \frac{\int_0^\infty yn(y)dy}{\int_0^\infty n(y)dy} \qquad (25)$$

gives

$$h_{\text{c.m.}} = \frac{kT}{mg} . \qquad (26)$$

This model therefore predicts the $1/N$ and $1/(1-\varepsilon)$ scaling observed by Luding, Herrmann, and Blumen [12] but not the $V^{3/2}$ dependence. We also find that kT/m scales as $1/d$, a point not noted by Luding, Herrmann, and Blumen [12].

There are several possible reasons why we do not get

the expected $V^{3/2}$ scaling predicted by Luding, Herrmann, and Blumen or the $V^{1.3}$ to $V^{1.4}$ scaling observed in our experiments. The assumption of an isothermal atmosphere and a uniform temperature right down to the shaker base are not strictly valid. In particular, the packing density deviates from the exponential form near the base, and the deviation becomes more important as V is reduced. The granular temperature is not constant, but shows significant decay with increasing height. Finally, the packing density is sufficiently high that the finite size of the grains should strictly be taken into account, for example, as in the van der Waals treatment of imperfect gases. Nevertheless, the model predicts the expected scaling behavior with N and ε, and is likely to prove a useful starting point for an improved theoretical understanding of vibrofluidized granular materials.

V. CONCLUSIONS

In this paper we have studied, both experimentally and theoretically, the behavior of a two-dimensional system of steel spheres undergoing vertical vibration. For a fixed frequency of 50 Hz, the effects of system size and vibration amplitude on packing fraction, speed and velocity distribution functions have been explored. By splitting the field of view into strips and cells, profile data for packing fraction and velocity distribution functions have been measured. The velocity distribution functions have been used to extract the granular temperature as a function of height in the cell. Three-dimensional surfaces show that the packing fraction profiles are fairly uniform across the cell with the degree of fluctuation increasing as the system size is decreased. Horizontal strip profiles show that a Boltzmann exponential distribution can be fitted to the packing fraction data when the bottom few strips are excluded. The Boltzmann distribution provides a good fit even though particle-particle collisions are inelastic. Inelastic collisions also mean that the energy input from the vibrating base will be gradually dissipated leading to a drop in granular temperature with height. Although the granular temperature profiles exhibit quite large fluctuations, due to small system sizes and short times of filming, a approximately linear gradient in

TABLE I. Summary of scaling exponents found in the experimental section. Comparison is also made with computer simulation results from Ref. [12] and with the simple theoretical model derived in Sec. IV. The text should be consulted for further details.

Method	Exponent α in $(A_0\omega)^\alpha$	Exponent β in $(n_b/N)^\beta$
Bulk speed distribution function	1.41±0.03	0.6±0.03
Boltzmann distribution tail fitted	Poor scaling results were obtained here, but the β exponent was closer to 1.0	
$h_{\text{c.m.}} - h_{\text{c.m.,0}}$	1.3±0.04	0.27±0.11
Simulation data from Ref. [12]	1.5±0.01	1.0
Theoretical model	2.0	1.0

granular temperature was observed.

Following recently published work [12] we considered the scaling behavior of the system granular temperature and height of the center of mass with vibration amplitude and system size. Experimentally, two approaches were used to measure the scaling exponents in Eq. (3) and the results are summarized in Table I. The three methods of estimating granular temperature are essentially equivalent in the ideal case of an isothermal atmosphere with Boltzmann density profile. However, as noted above, significant deviations from such a model are observed in practice due to inelasticity of the collisions and particle-wall friction, and it is therefore not surprising that different methods of estimating granular temperature result in slightly different scaling exponents. We also find that our exponents are lower than those found in computer simulation studies [12].

A simple theoretical analysis, based on elementary kinetic theory, leads to an expression for kT as a function of N, V, d, and ε. This model predicted kT to vary as $1/N$; as V^2; as $(1-\varepsilon)^{-1}$ for large ε, in agreement with the simulation results; and as $1/d$. This last dependency has not yet been checked, either by simulation or experiment, to the best of our knowledge. An improved model would need to take account of the significant deviations from the isothermal atmosphere.

[1] H. M. Jaeger and S. R. Nagel, Science 255, 1523 (1992).

[2] Chu-heng Liu and S. R. Nagel, Phys. Rev. Lett. 68, 2301 (1992).

[3] Chu-heng Liu and S. R. Nagel, Phys. Rev. B 48, 15 646 (1993).

[4] Chu-heng Liu and S. R. Nagel, J. Phys. Condens. Matter 6, A433 (1994).

[5] P. Evesque, Contemp. Phys. 33, 245 (1992).

[6] P. Evesque and J. Rajchenbach, Phys. Rev. Lett. 62, 44 (1989).

[7] E. E. Ehrichs, H. M. Jaeger, G. S. Karczmar, J. B. Knight, Vadim Yu. Kuperman, and S. R. Nagel, Science 267, 1632 (1995).

[8] S. Douady, S. Fauve, and C. Larouche, Europhys. Lett. 8, 621 (1989).

[9] H. K. Pak and R. P. Behringer, Phys. Rev. Lett. 71, 1832 (1993).

[10] E. Clement, S. Luding, A. Blumen, J. Rajchenbach, and J. Duran, Int. J. Mod. Phys. B 7, 1807 (1993).

[11] S. Luding, E. Clement, A. Blumen, J. Rajchenbach, and J. Duran, Phys. Rev. E 49, 1634 (1994).

[12] S. Luding, H. J. Herrmann, and A. Blumen, Phys. Rev. E 50, 3100 (1994).

[13] E. Clement and J. Rajchenbach, Europhys. Lett. 16, 133 (1991).

[14] C. S. Campbell, Annu. Rev. Fluid Mech. 22, 57 (1990).

[15] S. B. Savage, Adv. Appl. Mech. 24, 289 (1984).

[16] S. Warr, G. T. H. Jacques, and J. M. Huntley, Powder Tech. 81, 51 (1994).

[17] T. G. Drake and R. L. Shreve, J. Rheol. 30, 981 (1986).

[18] T. G. Drake, J. Fluid Mech. 225, 121 (1991).

[19] S. B. Savage, J. Fluid Mech. 194, 457 (1988).

[20] P. K. Haff, J. Fluid Mech. 134, 401 (1983).

[21] P. Evesque, E. Szmatula, and J. P. Denis, Europhys. Lett. 12, 623 (1990).

[22] J. Rajchenbach, E. Clement, and J. Duran, Int. J. of Modern Phys. B 7, 1789 (1993).

[23] G. T. H. Jacques, S. Warr, and J. M. Huntley (unpublished).

[24] B. Bernu, F. Delyon, and R. Mazighi, Phys. Rev. E 50, 4551 (1994).

[25] Y-h. Taguchi and H. Takayasu, Europhys. Lett. 30, 499 (1995).

[26] Y-h. Taguchi, in Numerical Methods in Multiphase Flows, ASME Fluids Engineering Division 195, 251 (1994).

[27] I. Goldhirsch, M-L. Tan, and G. Zanetti, J. Sci. Comput. 8, 1 (1993).

[28] S. Warr, J. M. Huntley, and G. T. H. Jacques (unpublished).